Preliminary design and analysis of crashworthy structures for a long-range eVTOL aircraft

Wadia, K.K.; Buszek, M.J.; Poliakov, M.; Castro, Saullo G.P.

DOI
10.2514/6.2022-1485

Publication date
2022

Document Version
Final published version

Published in
AIAA SCITECH 2022 Forum

AIAA SciTech Forum
January 3-7, 2022, San Diego, CA & Virtual
AIAA SCITECH 2022 Forum

10.2514/6.2022-1485

Preliminary design and analysis of crashworthy structures for a long-range eVTOL aircraft

Kaizad Wadia *, Michael Buszek †, Nikita Poliakov ‡, and Saullo G. P. Castro §
Faculty of Aerospace Engineering, Delft University of Technology, 2629 HS Delft, Netherlands

In aircraft structural design it is of utmost importance to minimise the structural mass while maintaining a durable structure that is able to sustain the design loads for a predetermined number of flight cycles. The present manuscript investigates a methodology for the preliminary design and analysis of a tandem-wing long-range electric vertical takeoff and landing (eVTOL) aircraft. First, a class I weight estimation for initial loads calculation is presented. Next, the flight envelope, main load cases and failure modes considered in this preliminary design are explained. Load approximations for the wing structures in cruise and take-off conditions are presented and discussed. Next, Cessna's class II semi-empirical weight estimation method is applied to calculate the mass of 11 eVTOL aircraft subsystems. A design concept for the wing tilting mechanism is proposed. Thereafter, an initial fuselage layout design is presented, followed by a discussion on design for crashworthiness. The aeroelastic behaviour of the wing and the whirl flutter considering the propeller engine structures is investigated. Lastly, refinements in the design parameterization are implemented concerning the thickness distributions in the structural elements of the wingbox, and finally a sizing of the wing rotating shaft is performed.

I. Introduction

The structural design of eVTOL aircraft involve vertical takeoff, transition between vertical and horizontal flights and vertical landing that are relatively novel concepts, for which literature on the design and analysis of crashworthy lightweight structures is scarce. For long-range eVTOL, it is also usual to have a tilting wing or tilting rotors such that the same propulsion system can be used during all flight conditions.

The present study consists of a preliminary design and analysis of crashworthy structures for a tandem-wing long-range eVTOL aircraft, named Wigeon. The aircraft features two horizontal wings of equal area positioned at the front and rear parts of the fuselage, has leading edge open rotors, a capacity of four passengers and one pilot, a range of 400 km, and is fully electric. The transition between horizontal and vertical flight is achieved via the rotation of the wings. The final configuration can be seen in Figure 1.

Fig. 1 Rendering of the final design of the analysed configuration of the Wigeon.

The proposed characteristics were obtained from a market analysis conducted during the project, assuming a market

*Corresponding author, MSc student, ORCID: 0000-0002-8984-7958, email: kaizad.wadia21@imperial.ac.uk
†Corresponding author, MSc student, email: M.J.Buszek@student.tudelft.nl
‡Corresponding author, MSc student, email: M.Poliakov@student.tudelft.nl
§Corresponding author, Assistant Professor, ORCID: 0000-0001-9711-0991, email: S.G.P.Castro@tudelft.nl

entry in 2030, as further detailed in the original project report [1]. Furthermore, the Wigeon has been designed with the objective of easy market introduction, without requiring an extensive infrastructure for its operation, nor extensive certification campaigns for critical systems. As such, the selected power source was that of batteries instead of hydrogen [2] and its size is limited to be operable in existing helipads, for which all horizontal dimensions are constrained to be below 14 m [1].

The present study describes the steps followed during the preliminary structural design and analysis, starting with the mass estimation, followed by the load calculation and analysis of the wings. Thereafter, the material selection is discussed and the component mass estimation is conducted along with the estimation of their corresponding centre of gravity. After that, the fuselage is designed and its connection with the wing is explained along with a preliminary discussion on how the wing rotates and a proposed mechanism for the tilting motion. Finally, the crashworthiness and aeroelastic characteristics are analysed before concluding the manuscript, while looking into improvements that can be made to preexisting methods.

II. Preliminary mass estimation

Using data from a recent review of current technology and research in urban on-demand air mobility applications [3]; and a database of eVTOL configurations [4]; the two regression lines shown in Figure 2 were obtained for operational empty mass versus maximum takeoff mass; and for maximum takeoff mass versus the payload. The data includes short-, medium- and long-range eVTOLs, which is not ideal for the estimation of the long-range eVTOL mass herein investigated. Using Figure 2, it is possible to find the required maximum takeoff mass based on a desired payload. Assuming a payload requirement of 475 kg [1], corresponding to four passengers of 95 kg each and the pilot, the values $MTOM = 1930.62\ kg$ and $OEM = 1565.15\ kg$ are directly obtained; which are used as preliminary mass estimation values necessary for the initial load calculations.

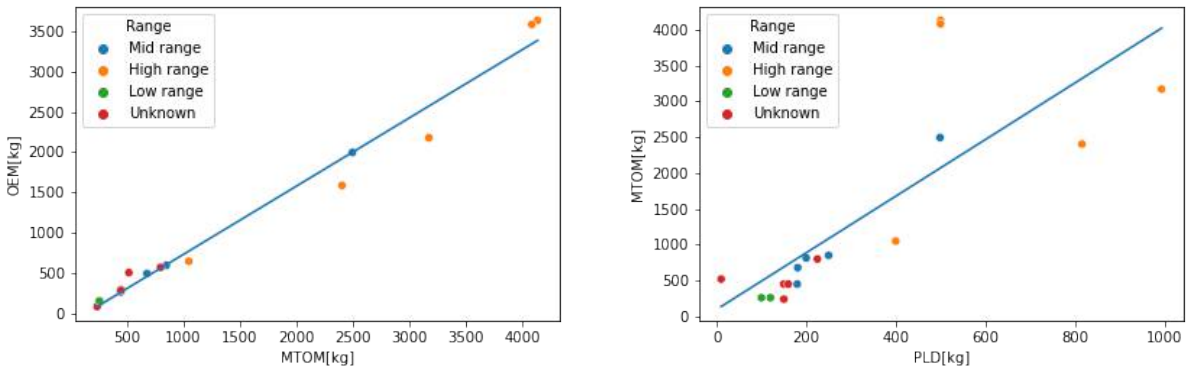

(a) Takeoff mass versus operational empty mass **(b) Payload versus takeoff mass**

Fig. 2 Preliminary mass estimation curves.

III. Flight envelope

To compute the loads acting upon the aircraft in flight, a gust loading diagram and a manoeuvre loading diagram is created. When computing the gust loading diagram Equation 1 is used, wherein u is the gust velocity, V is the flight velocity, and W/S is the wing loading. Three gust loads given by certification specifications (CS) [5] are respectively $ub, uc, ud = 20.12, 15.24, 7.62$ m/s; and three design velocities are determined, namely, design velocity for maximum gust intensity, cruise and dive. The interpolation of the points and Equation 1 (left) provide the basis for the gust loading diagram. For manoeuvre loading diagram, the approach is slightly different, with the loads corresponding to the stall speed computed using Equation 1 (right):

$$n = 1 \pm \frac{\rho \cdot V \cdot C_{L_\alpha} \cdot u}{2 \cdot W/S} \qquad n = \pm \frac{0.5 \cdot \rho \cdot V^2 \cdot C_{L_{max}}}{2W/S} \tag{1}$$

The quadratically increasing line is then cut off at the maximum allowable load factor, which is set by the CS. The n_{upper} in the case of the Wigeon eVTOL is 2.5. The same procedure is applied for negative load factors, where n_{lower} is -1, also set by the CS. The maximum possible aircraft speed is defined as the dive speed, V_D, which defines the right-hand side limit of the flight envelope.

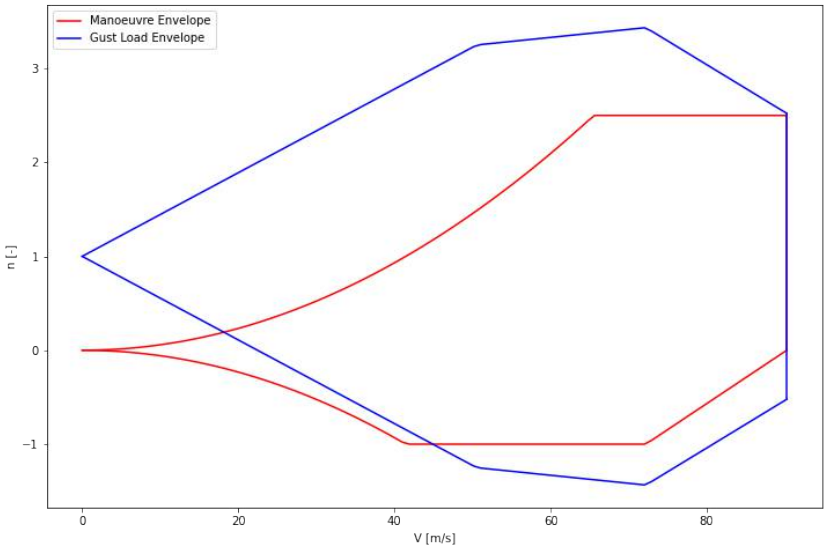

Fig. 3 The flight envelope

Both the manoeuvre and load diagrams are defined for a specific altitude, which here is the design cruise altitude, given that this is the altitude at which the aircraft spends the majority of its mission time. The diagrams are then combined and the maximum load factor is determined, resulting in Figure 3. It follows that, the maximum limit load factor that the structure has to withstand is 3.2 without failing, which is a reasonable result, considering that it is common for CS-25 transport aircraft to reach a limit load factor of 2.5. Moreover, this maximum limit load factor is multiplied by 1.5 to reach the so-called ultimate load factor, where the structure should not critically fail, and structural damage such as localized failures or permanent deformation may occur, given that the aircraft remains operational to complete a safe landing.

IV. Load cases and failure modes

In order to design and analyse the structure, it is important to know what the structure is being designed for. The necessary approach is to identify and analyse critical load cases where the limits of the structure are tested. One of such cases is gust and manoeuvre loads during cruise, described in subsection IV.A. Another case is the vertical takeoff, described in subsection IV.B.

Initially, a rectangular wingbox is analysed with a number of stiffening elements for the above stated load cases. Despite several critical failure modes are to be analysed, it is found that for most aircraft components, the three most common causes of failure are fatigue, corrosion and overload, in that order [6]. When it comes to overload, bending moments, shear forces and critical buckling stresses are analysed. For fatigue, the variable amplitude load cycle is analysed using several semi-empirical methods including the S-N curve, Paris' law and Miner's rule to determine its fatigue life and damage tolerance. Lastly, for a preliminary assessment on corrosion, several aspects are discussed in terms of their relevance to the material selection and operational considerations. [7]

For overload, the bending loads are computed using the bending stresses equation, assuming a linearly elastic material. Additionally, a symmetric wingbox is assumed, such that term $I_{xy} = 0$. The moment of inertia, being a geometric property, is trivial to compute with a set of rectangles and their Steiner terms. For shear flows and stresses, Equation 2 is used, which gives the shear flows and bending stresses through a cross section with an axis of symmetry

(ie. $I_{xy} = 0$):

$$\sigma_z = \frac{M_x y}{I_{xx}} + \frac{M_y x}{I_{yy}} \qquad q_2 - q_1 = \int_{s1}^{s2} \frac{\delta q}{\delta s} ds = -\frac{V_y}{I_{xx}} \int_{s1}^{s2} tyds - \frac{V_x}{I_{yy}} \int_{s1}^{s2} txds \tag{2}$$

Since the wing box has a closed cross section, it needs to be 'cut' somewhere in order to analyse the section like an open one. Luckily, due to symmetry, cutting the in the middle of the bottom flange and the middle of the left web does not introduce any redundant shear flows, since they are 0 in these points, thus simplifying the calculation.

Adding shear flow due to torque is trivial, as it is simply $q = T/2A$, where T is torque and A is the enclosed area. All the shear flows are superimposed and the shear stresses are then easily found by simply diving the flow at the specific location by the corresponding thickness.

The buckling allowable of the upper panel is computed using the equation:

$$\sigma_{cr} = C \frac{\pi^2 E}{12(1-\nu^2)} \left(\frac{t}{b}\right)^2 \tag{3}$$

where E is the Young's modulus, ν is the Poisson ratio, t is the thickness of the plate and b is the side where the impressive load is not applied; C is a function of the aspect ratio and boundary conditions of the plate. The top plate of the wingbox under analysis is assumed to be clamped at the root and to be simply supported on other sides, which makes $C = 5.41$. The simply support assumption leads to conservative estimates and makes the analysis less dependant on the geometry of the stringers.

An investigation of stringer geometries is conducted on a reference wingbox composed of aluminium 2024-T4 with 8 stringers of same cross sectional area of 130 mm^2. It is discovered that out of the Hat-, Z-, and J-shaped stringers the best performing one is the Hat stringer, becoming the chosen cross section to be used in the sizing optimization.

As mentioned before, fatigue is analysed using semi-empirical relations to provide a preliminary design that is fatigue resistant and fault tolerant[7]. These equations assume constant amplitude fatigue loading and are used in estimation of crack growth and crack initiation. However, the real loads on the aircraft are not of constant amplitude, meaning that to simulate the loads accurately the loads on the aircraft have to be converted from varying amplitude to a series of constant amplitude loads. This is done using the rainflow cycle counting method, and later assimilated with Miner's rule (Equation 4) or the coalescence of cracks (Equation 5). While this method permits the use of conventional semi-empirical loads for the design, the major caveat is that information regarding the order of the loads is no longer preserved. Once the discrete single amplitude loads are analysed by the SN-curve, their design lives can then be consolidated to a single design life cycle, with D in Equation 4 being the proportion of the design life elapsed in one ground-air-cycle. This can then be reciprocated to find the number of ground-air-ground cycles until the design life is reached.

$$D = \sum_i \frac{n_i}{N_i} \tag{4}$$

$$a_f = a_0 + \sum_i \Delta a_i \tag{5}$$

The loads on the aircraft are categorised as either stochastic or deterministic. The deterministic loads are evaluated with the mechanical analysis described above. The stochastic loads are assumed to follow a Gaussian distribution with a standard deviation of roughly $1/3$ of the difference between the mean (zero) and maximum. This then used a normalised Fourier series to simulate the loads at varying frequencies, obtained from literature [7].

$$A(t) = \sum_i A_i \sin(2\pi f_i t) \tag{6}$$

For crack initiation, a simple S-N curve, otherwise known as Wöhler's curve, is used for aluminum 7075-T6, which is the material chosen. The construction of a S-N curve, such as the one shown in Figure 4, requires an experimental campaign; and there are methods to apply this curve semi-empirically. The relationship in Figure 4 is described by the Basquin's Law, as ${S_a}^m \cdot N = C$, where S_a is the load level, $m = 4.10$ and $C = 3.15 \cdot 10^{14}$, which depend on material properties [8]. Note that the scale is logarithmic, such that a small variation in the stress level leads to a large variation in the fatigue life. Using this relationship, it is possible to estimate the fatigue life of the selected concepts for different load levels.

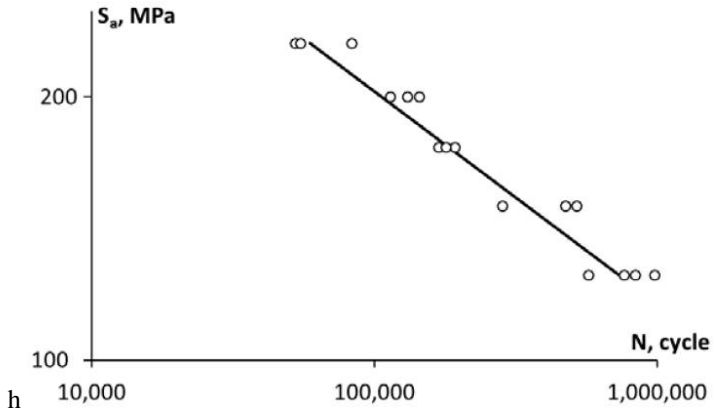

Fig. 4 The S-N curve for 2024-T3 aluminium alloy under axial tension-compression [8].

Paris' law is used to predict fatigue crack growth in a structure under constant amplitude loads.

$$N_{a_0 \to a_f} = \int_{a_0}^{a_f} \frac{1}{f_R(\Delta K)} da \tag{7}$$

where a is the crack length, and $f_R(\Delta K)$ represents crack growth resistance of the material.

$$\frac{da}{dN} = C\Delta K^m = C(\beta \Delta\sigma \sqrt{\pi a})^m \tag{8}$$

Substituting Equation 8 into Equation 7 results in:

$$N = \frac{1}{C\Delta\sigma^m} \int_{a_0}^{a_f} \frac{1}{(\beta\sqrt{\pi a})^m} da \tag{9}$$

In the equations above, β is a geometry factor related to crack propagation, m is the Paris exponent and C is the Paris constant, both are dependent on the material. The initial crack length is chosen to be $0.375 \cdot 1.2$mm as this is the smallest length that can be detected by the mechanoluminescence film [9]. Furthermore, this model does not account for plasticity induced crack closure, which is modelled using the Elber mechanism [7] for Aluminium 2024-T3, given by the equation [7]: $\Delta K_{eff} = (0.5 + 0.4R)\Delta K = (0.5 + 0.4R)\beta\Delta S\sqrt{\pi a}$, where R is the stress ratio. Therefore, ΔK_{eff} is used in the calculations instead of ΔK. The final crack length is chosen to be half of the thickness of the wingbox thickness. Parameter β is defined as 1.125 with the assumption that the crack is initiated at the top right corner of the plate, as this case is more critical than cracks in the centre of the material. The number of cycles is then determined numerically using numerical integration.

A. Cruise

For the cruise flight condition, the maximum positive load factor from Figure 3 is considered. The loads on the aircraft are shown in Figure 5, with values of some parameters taken from the results other disciplines, to be included in the final manuscript, or from the preliminary mass estimation explained earlier. These loads are first solved for a simple longitudinal equilibrium situation, and the solved values of those loads are then applied on the wing's aerodynamic centre line to create a distribution of shear forces and bending moments (NVM diagrams) as well as internal torque along the half span of the wing. For this, the weight of the wing is assumed to be uniformly distributed along the spanwise direction. The aerodynamic force distribution is obtained from the aerodynamic analysis of the wing [10]. Buckling of the upper panel is the identified as a critical failure mode in cruise.

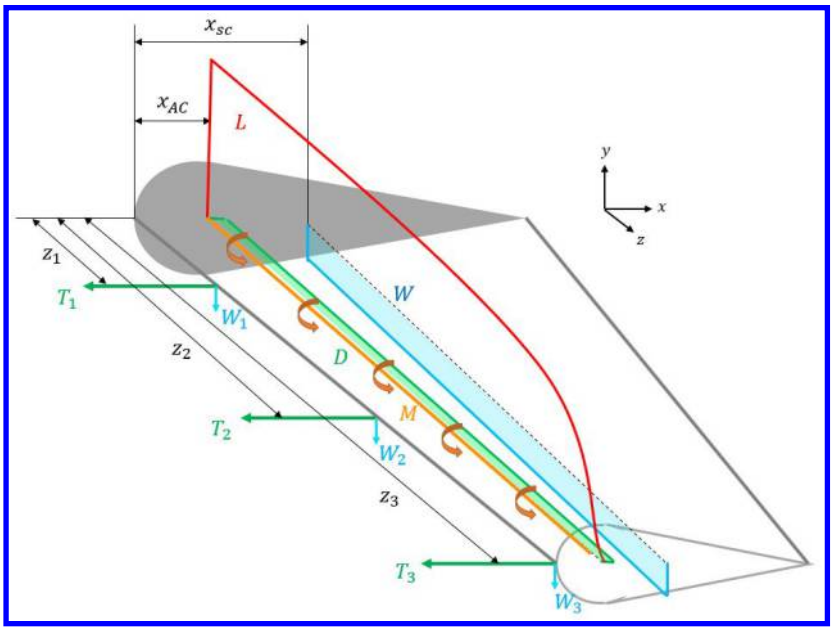

Fig. 5 FBD showing all aerodynamic loads at horizontal flight.

Table 1 Stresses occurring in the wing root under loads in cruise.

Bending axial stress (σ)[MPa]	58.26
Critical buckling stress (σ_{crit})[MPa]	63.76
Number of cycles (Crack Growth) [10^6]	1.116
Shear stress (τ)[MPa]	268.57
Number of cycles (Initiation) [10^6]	135.848

B. Vertical takeoff

For the vertical takeoff condition, the wings or engines are rotated and maximum thrust is applied, as this would be the most critical situation to analyse during takeoff. These situations are depicted in Figure 6. The results from the numerical structural analysis are given in the Table 2. Critical buckling and life cycles are omitted since both of these take bending stresses as inputs, compression of the top plate for buckling and cycling between compression and tension of the plates for fatigue. Since the bending stresses stresses for this situation are several times lower than those for cruise, fatigue or buckling would not be critical in this situation.

Table 2 Stresses occurring in the wing root under loads in vertical takeoff.

Bending moment (σ)[MPa]	23.0
Shear stress (τ)[MPa]	3.6

It is evident that the stresses during vertical takeoff are much less severe since maximum thrust is roughly equal to the weight of the aircraft. During cruise, the lift is approximated by multiplying the weight by the ultimate load factor.

V. Aircraft material selection

In order to select the material, a material index is derived using a cost function that is essentially based on the structural mass. As the wing is designed to be lightweight and loaded in bending, the material index is equivalent to that of a single lightweight stiffened panel. Therefore, the material is chosen to minimise the cost, $\rho \cdot E^{-1/3}$. Through a data

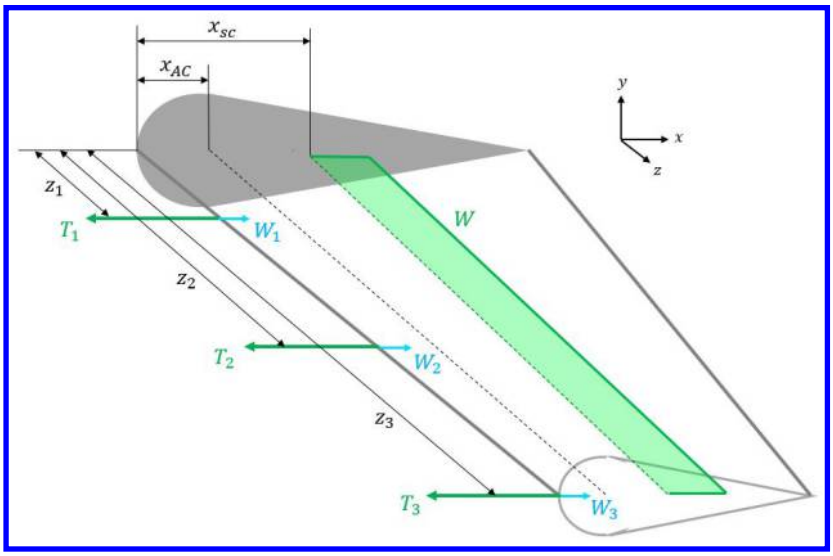

Fig. 6 Free-body diagram for the vertical flight.

analysis on over 100 metal alloys, the optimal one to be selected was Aluminum 7075-T6 since it is one of the best performing metals but also has a particularly high yield strength of 468 MPa. That is why it is employed for all structural components. In addition, Aluminium 2024-T3 is used for the skin as it has favorable corrosion and fatigue properties.

With the selected material in mind, the structure's susceptibility to corrosion are taken into consideration, particularly localised and galvanic corrosion. As aluminum alloys are in general resistant to uniform corrosion, uniform corrosion has not been investigated. Localised corrosion is an attack on a specific region, in contrast to uniform corrosion which affects the entire surface. Aluminum 7075-T6 is particularly susceptible to localised forms of corrosion including pitting and crevice corrosion and is also soft and prone to wear [11]. This makes the operations and repairs more critical than for other alloys that have a failure mode that is easier to predict. This means that regular inspections must be performed in addition to those regarding fatigue cracks in order to assess possible locations of wear. A further effort also needs to be made so that fatigue does not exacerbate the structural deformities due to pits. Galvanic Corrosion is the corrosion of dissimilar metals in the presence of an electrolyte [6]. The definition of "dissimilar" is in varying positions on the galvanic series, which is an ordered sequence of metals by their steady state potential. The presence of galvanic corrosion thereby incentivises the use of as few materials as possible, which is why most load bearing structural components are to be composed of Aluminium alloys.

VI. Aircraft component mass and centre of gravity estimation

The class I estimation curves of Figure 2 provide a useful first estimate of the operational empty mass that can be used for the first load calculation. During the preliminary design cycles, this initial estimate of the mass can be further refined. The estimation of the mass for various components of eVTOL aircraft has not been extensively investigated, given the large variety and novelty of the different eVTOL concept. Therefore, a method of semi-empirical estimation is used to estimate the wing and fuselage weights. The estimation methods used are taken from a book by Dr. Jan Roskam [12]. The specific method used is applied for general aviation airplanes and is known as the "Cessna method".

The wing weight is estimated using the following equation:

$$W_w = 0.04674(W_{TO})^{0.397}(S)^{0.360}(n_{ult})^{0.397}(AR)^{1.712} \tag{10}$$

where W_{TO}, S, n_{ult}, AR are respectively takeoff weight from class I estimation (section II), wing area, ultimate load factor and aspect ratio. For tandem and box wing configurations, the area and aspect ratios are considered separately for each wing, and then are added to the wing group.

The fuselage weight is estimated using the following two equations:

$$Wf_{lowwing} = 0.004682(W_{TO})^{0.692}(P_{max})^{0.379}(l_{f\_n})^{0.590} \tag{11}$$

Table 3 Mass fractions for eVTOL components.

	Mass [kg]	% of OEM	% of MTOM
Front wing	174.9	12.2	6.3
Back wing	174.9	12.2	6.3
Fuselage	210.6	14.7	7.5
Vertical tail	14.9	1.0	0.5
Passengers	440.0	0.0	15.8
Furnishings	98.4	6.9	3.5
Electronics	131.6	9.2	4.7
Cargo	35.0	0.0	1.2
Battery	886.2	0.0	31.8
Landing gear	121.0	8.5	4.3
Propulsion	502.6	35.2	18.0
Total Mass		1428.9 kg	2790.1 kg

$$Wf_{highwing} = 14.86(W_{TO})^{0.144}\left(\frac{l_{f\_n}}{P_{max}}\right)^{0.778}(l_{f\_n})^{0.383}(N_{pax})^{0.455} \tag{12}$$

where $P_{max}, l_{f\_n}, N_{pax}$ are fuselage length, maximum perimeter of the fuselage and number of passengers, respectively. For the Cessna method, the pilot and any crew members are included in the number of passengers. For a tandem or box wing configurations, both formulas are used to compute the weight of the fuselage and the average is taken to account for both wings. Using the above listed formulas and the relevant values, the component weight fractions shown in Table 3 are calculated.

These values are obtained through one iteration. However, since semi-empirical methods are used to calculate the masses, these do not take into account unconventional configurations such as the present eVTOl aircraft. For instance, the method does not take into account the fact that a vertical takeoff propeller is used, which would significantly change the weight of the wing. The mass estimation method herein proposed starts with a preliminary estimation using the class I method given by Figure 2, adopts a class II with more accurate mass estimates for individual components, and also allows to replace individual mass fractions given in Table 3 by calculated values.

VII. Fuselage initial design

The following constraints on component sizes are collected from the previous design iteration and requirements [13]: The headroom height measured from the floor should be 1.5 m, the height at the passenger's shoulder should be at least 0.95 m, the seat pitch should be around 0.8 m and the width of a seat 0.6 m. The chosen configuration is a simple 2 rows of 2 passengers, with a separated single-seat cockpit in the front. The initial cabin layout is shown in Figure 7.

The choice to face the front 2 seats backwards is made to reduce the necessary number of passenger cabin doors from 4 to 2 as this change reduces the weight of the aircraft due to the mechanisms of the additional two doors and the increase in strength of the structure due to having fewer discontinuities at the locations of the doors. Additionally, the cockpit is designed to be 1 m long to allow for the pilot's seat and the controls and dashboard. For aerodynamic reasons [1, 10], the fuselage cross section is the smallest multi-arc oval-like shape wrapped around the necessary inside space. The cross section of the passenger cabin can be seen on the right of Figure 7. Behind the passenger cabin is the tail curve, which decreases the cross section area gradually to prevent excessive boundary layer separation and pressure drag. The cargo compartment is positioned inside this tail, filling up most of the empty space. There is also empty space below the cabin floor, which can be used either for batteries or for an energy absorbing structure. This trade-off is further discussed in section IX.

The width of the fuselage is 1.3 m, the length is 4 m and the height is 1.6 m.

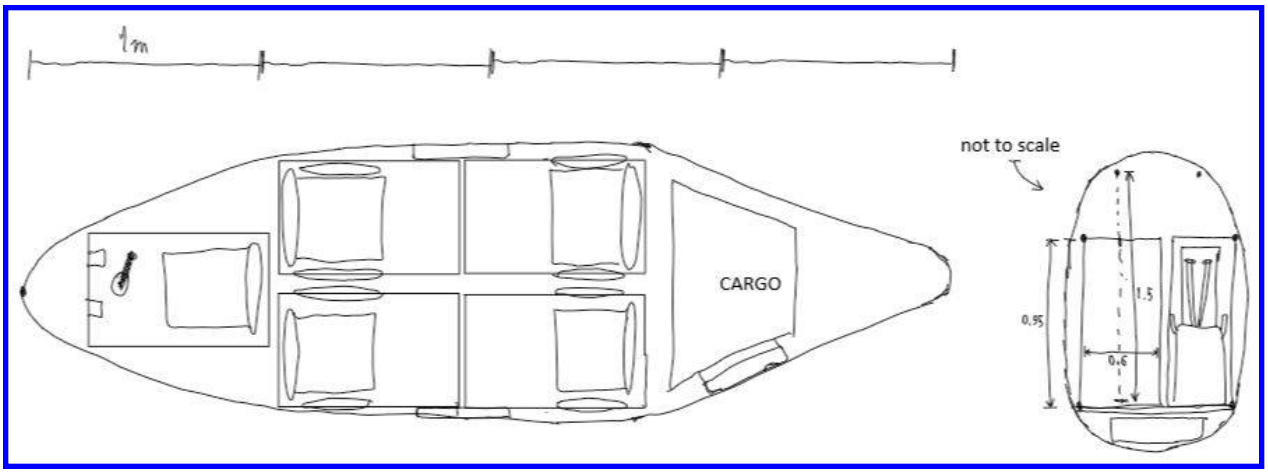

Fig. 7 Drawing of initial fuselage design

VIII. Wing rotation Mechanism

One important requirement for the wing rotation mechanism is that the right and left wings must be rotated at the same angle at all times, to reduce the number of possible failures in hover mode. The rotation mechanism also needs to be precise and be able to lock in the hover and cruise positions. It is also required for the mechanism to reach a sufficient rotation speed of a right angle in 3 seconds. Above all, the probability of failure must be sufficiently small during the transition from horizontal to vertical flight.

In the present work it is proposed that all these requirements are met using a simple worm gear powered by an electric servo. It is precise, self-locking because it prevents back drive, reliable, and it can power a shaft that rotates on both sides of a wing simultaneously.

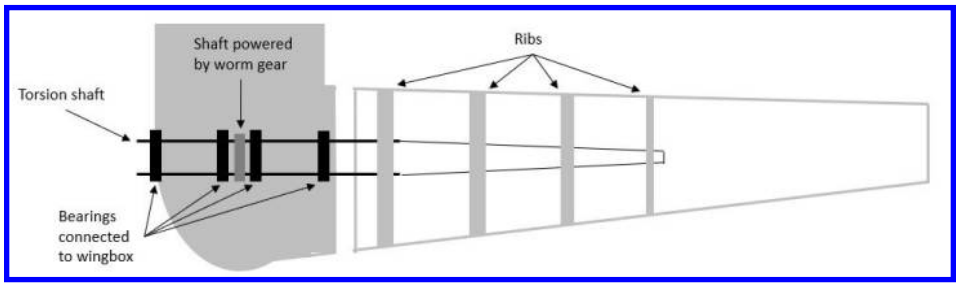

Fig. 8 Wing rotation mechanism sketch

As can be seen in Figure 8, the worm gear spins the output gear, which is connected to a hollow circular torsion shaft passing through the inside of the central wingbox section. The central wingbox from Figure 8 is not attached to the main gear. The wingbox stays in place while the gear and shaft rotate inside of it. The electric servo spinning the worm gear can be attached to the wingbox surface or to a separate fuselage frame if needed. As seen in Figure 8, the translation of the aforementioned shaft is constrained to the central wingbox by bearings, but it's still free to rotate with respect to the wingbox. The use of those bearings has two goals: to prevent the shaft from bending and disconnecting the gears, and to transfer some bending loads from the shaft to the central wingbox. Going into the rotating part of the wing, the shaft connects rigidly to multiple ribs in the wingbox to gradually introduce the loads into the structure. This is also illustrated in Figure 8.

The most critical part of the shaft is where the central wingbox is connected to the outside wingbox, where all the bending loads are carried by the shaft. In the preliminary design, the shaft is designed to be placed at the quarter chord position to be roughly coinciding with the aerodynamic center.

IX. Crashworthiness

A crashworthy vertical takeoff and landing (VTOL) vehicle design is defined by its ability to protect its payload from harm during a ground impact. From past incident analysis it is known that injury during a helicopter crash comes from excessive acceleration during impact, a contact injury by a body part hitting a hard surface, and environmental injuries such as from fire, smoke or water [14].

Environmental injuries are not considered for now; and similarly, injury from impact of body parts on hard surfaces is assumed to be prevented, by including seat harnesses and ensuring the fuselage structure is strong enough not to collapse onto the passengers.

For single wing VTOL vehicle, the safest wing placement is a low wing, because a high wing leads to extra mass above the passengers that has to be decelerated by the structure during a crash. A low wing configuration therefore allows for lighter fuselage structure with respect to crashworthiness. However, there is a major disadvantage to the single wing configuration. For aerodynamic stability and controllability, the wing must be positioned close to the centre of gravity, which for a low wing happens to be below the passenger cabin, and stiff lifting structures underneath the cabin can negatively affect the crashworthiness behaviour, so one must guarantee enough energy absorption for these structures in the event of a crash. In other words, the space under the passenger cabin would be better used for an energy absorbing structure to protect passengers from excessive impact acceleration. The proposed tandem wing configuration for the Wigeon allows the wings to be positioned in extreme front and aft locations of the fuselage, decoupling the required stiffness of the wings structures and tilting mechanism from the crashworthiness behaviour of the fuselage.

The rear wing of the Wigeon is located above the cargo compartment. Given that no valuable payload is stored under the rear wing, the aforementioned disadvantage of a high wing can be ignored. The front wing, however, creates a stiff structure under the pilot's seat, which might be still a problem for crashworthiness, although less critical than the stiff wing under the passenger cabin in the hypothetical single wing concept. Possible solutions to protect the pilot during a crash are a special energy absorbing seat assembly [14], or an ejection seat for the pilot to use just before impact. Such solutions should be investigated in a more detailed design phase.

In the case of electric VTOL aircraft, batteries are also stiff elements that should not be placed below the passenger's cabin due to crashworthiness. Additionally, batteries might catch fire after a crash, and therefore one should try to keep them away from passengers. Those two factors imply that it is beneficial to carry the batteries in the wings [15].

Next, the landing gear is designed to absorb as much energy as possible while not puncturing through the cabin. The rest of the energy is absorbed by energy absorbing materials placed below the cabin, by the cabin structure and the seats. There are multiple options for such energy absorbing materials, such as metal rings, tubes, or a hexagonal matrix [14]. The energy absorption mechanism must guarantee a maximum specific energy absorption whereas keeping a minimum peak deceleration.

To prevent injury to regular passengers, not necessarily sitting in perfectly upward positions, the maximum deceleration is limited to less than the 20g in a time frame of 0.1 s. Therefore, the deceleration of the cabin has been constrained to 8g for landing gear and to 11g for the energy absorbing structures. The landing gear is modelled as a 2D state-space system, with 2 spring-damper assemblies placed on a line, each spring damper assembly symbolising a set of 2 symmetrically placed landing gears.

The model is governed by the equations of motion represented in Figure 9, with $f(t)$ modelling the impact momentum by means of a Dirac delta function. These equations are converted to a state space system and solved for a time response of y, β and $\ddot{y}$; using the planform parameters supplied in Table 4. It can be seen that, after modelling the impulse response using these parameters, passengers would endure a maximum acceleration of 2.2g in the limit crash case of a vertical drop at 9.9 m/s.
where $y1$, $y2$, $y3$, $y4$ are the vertical displacements of each landing gear.

In the case that the load is much greater than 8g, the landing gear is likely to fail and so an energy absorbing structure is proposed to provide further protection for the passengers in these circumstances. The aim of the energy absorbing structures is to limit the deceleration on impact to 11g, excluding a short initial peak of much larger acceleration. After researching aluminium, aramid and glass-fibre honeycomb structures, the aramid composite material is chosen for its low density. The product with the lowest stabilised compression strength (0.6 MPa) from the aramid structures from HEXCEL [16] is chosen, so that the deceleration loads can be distributed along a greater area; and if the available area is exceeded, a stronger layout can be chosen, such that the proposed solution can be easily adapted towards more detailed design phases. From composite honeycomb structure crushing experiments [17], it can be found that the crushing stress for a honeycomb structure is around 23 % of the stabilised compression strength. The area of the crashing structure is determined as 1.39 m^2, which is distributed in a strip along the middle of the cabin length, to allow space for the front landing gears next to the pilot. The strip dimensions are summarised in Table 5. With a density of 23 kg/m^3, the entire

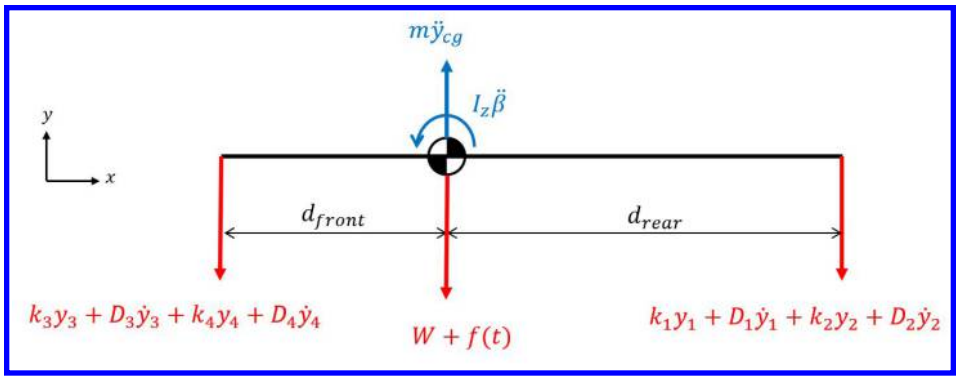

Fig. 9 The free body and kinetic diagram for the landing gear model

Table 4 Model Parameters

Parameter	Values
d_{rear} [m]	2.35
d_{front} [m]	0.85
l_{strut} [m]	0.4
k_1, k_2 [N/m]	40100
k_3, k_4 [N/m]	80200
D_1, D_2 [Ns/m]	4050
D_3, D_4 [Ns/m]	8100

energy absorbing structure has negligible mass, as computed from the volume using the dimensions from Table 5.

Table 5 Strip dimensions

Parameter	Values
w_{HEX} [m]	0.375
l_{HEX} [m]	3.70
h_{HEX} [m]	0.167
m_{HEX} [kg]	5.3

This preliminary assessment leads to the conclusion that an optimally crashworthy design stores all batteries in the wings, keep the wing structures or other lifting structures away from the cabin, has properly designed landing gear to absorb energy while not puncturing through the cabin, uses energy absorbing structures between the lower fuselage skin and the cabin floor, and optionally features energy absorbing seats.

X. Aeroelasticity

The investigation of flutter involves understanding the dynamic response considering inertial, elastic and aerodynamic forces. Two kinds of flutter are herein explored, being the wing divergence and the propeller whirl flutter. The wing geometry is assumed to be a thin-walled rectangle, with a mass moment of inertia about the axis which it rotates. For whirl flutter, the propeller and connection geometry is modelled as a rotating disk on a cylinder. These are consolidated using their individual moment of inertia terms due to the parallel axis theorem, which is the product of their mass and the square of their distance to the axis about which they rotate: $M \cdot d^2$.

Divergence is an aerodynamic phenomenon through which the lift on the wing increases the angle attack due to the deformation, thus amplifying the lift. This is analogous to the superposition of a vertical and torsional coupled spring-damper system. On the other hand, whirl flutter is the unstable angular motion of the propeller due to the

moments about its pitch and yaw axis. The divergence is modelled using the governing equations of the free body and kinetic diagram in Figure 10. The motion of whirl flutter is shown in Figure 11.

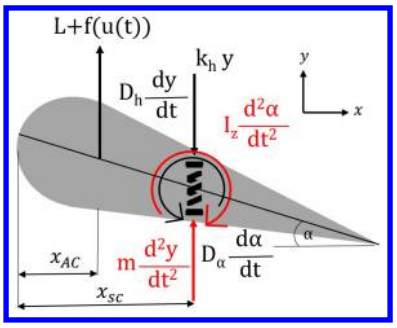

Fig. 10 Free body & Kinetic diagram

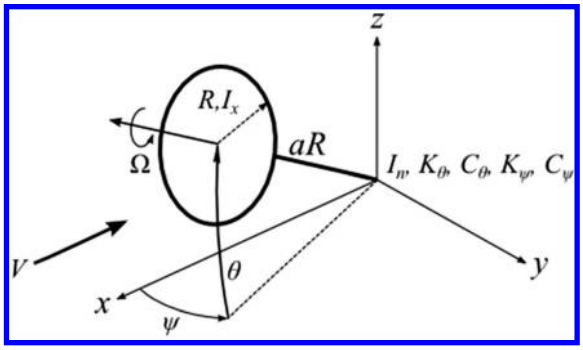

Fig. 11 Propeller Motion two degrees of freedom [18]

After performing a sensitivity analysis over a large range of gusts, spanwise positions, damping constants and velocities, it became apparent that wing divergence is not a critical failure mode as the system is well damped for a damping ratio, $\zeta = C/(2\sqrt{km})$ of around 2%. Furthermore, the design dive speed is significantly lower than the speed at which flutter is likely to be observed.

Propeller whirl flutter is described by Equation 13, where I_x represents moment of inertia about the axis of rotation of the propeller and I_n the axis about the pitch and yaw directions. These are equivalent due to the circular symmetry of the assumed geometry. Parameter Ω represents the angular velocity of the propeller, and M represents the moments applied thereto in each direction. The moments were computed by integrating the lift over the propellers using the propeller's geometric properties given their aerodynamic coefficients as mentioned in [18]. Finally, K denotes the stiffness of the equivalent spring in the direction specified by the subscript and C the damping coefficient. These equations were then placed in a state space form before being numerically solved. The solution is found for the vertical takeoff condition as the weight of the propeller is not taken into consideration, and the free stream velocity is set to 5 m/s. This is the critical condition for whirl flutter, in which the vibrations of the propeller can adversely affect the aircraft structure.

$$\begin{bmatrix} I_n & 0 \\ 0 & I_n \end{bmatrix} \begin{bmatrix} \ddot{\theta} \\ \ddot{\psi} \end{bmatrix} + \begin{bmatrix} C_\theta & -I_x\Omega \\ I_x\Omega & C_\psi \end{bmatrix} \begin{bmatrix} \dot{\theta} \\ \dot{\psi} \end{bmatrix} + \begin{bmatrix} K_\theta & 0 \\ 0 & K_\psi \end{bmatrix} \begin{bmatrix} \theta \\ \psi \end{bmatrix} = \begin{bmatrix} M_\theta \\ M_\psi \end{bmatrix} \tag{13}$$

It is found that the system is damped for the chosen angular velocity of 4000 RPM when the propeller is supported by a certain thin-walled rod, which is made of annealed steel AISI 4140; and has a thickness of 1 cm, outer radius of 10 cm and length of 38.2 cm.

XI. Tapered wingbox and bending shell buckling of the tilting shaft

After the preliminary design, the modelling techniques employed are improved by including a linear tapering of the thickness of the wingbox skin and spar along the spanwise direction, enabling further weight reduction. Moreover, a sizing of the wing rotating shaft mentioned in section VIII is performed.

The wingbox is sized at two critical points, determined to be the root of the wing, and at 2.6 m away from the root, i.e. at 5/8 of the half-span). The thicknesses at the root would axiomatically be equivalent to:

$$\vec{t}_0 = (1.3, 18.7) \qquad \vec{t}(z) = (t_{sk}, t_{sp}) = \vec{m} \cdot z + \vec{t}_0 \tag{14}$$

where t_{sp} is the thickness of the spar, t_{sk} is the thickness of the skin and z is the coordinate along the spanwise axis. By computing the thickness at z = 2.6 m to be $\vec{t}(5b/16) = (0.69, 7.5)$ mm, it could be determined that $\vec{m} = (-0.238, -4.366)$ mm / m; and therefore the thicknesses at the tip are computed to be $\vec{t}_{\text{tip}} = (0.324, 0.78)$ mm. It is thereby evident that this reduction in thickness along the spanwise direction results in considerable weight savings due to the reduction in volume while satisfying the requirements.

Another refinement is the use of a circular shaft to carry the loads and rotate the wingbox about the quarter chord line. In order to do this, the tubular cross section is placed along the aerodynamic center of the wing and the loads

acting upon it are computed using the same method as described in section IV (with the same loads, but with a different geometry. In this case, shell buckling under bending is found to be the dominant failure mode. This failure mode is calculated using the following equations, where γ denotes a geometric factor composed of the outer radius R, and the thickness of the tube t:

$$\gamma = 1 - 0.731 \cdot \sqrt{1 - e^{-\phi}} \qquad \phi = \frac{1}{16}\sqrt{\frac{R}{t}} \tag{15}$$

Then, the critical normal and shear stresses due to bending and torsion could be respectively defined in terms of γ, the Young's Modulus E, the Poisson's ratio ν, and the length of the beam L, such that:

$$\sigma_{cr} = \gamma \cdot \frac{Et}{R\sqrt{3 \cdot (1 - \nu^2)}} \qquad \tau_{cr} = \frac{0.747 \cdot \gamma^{0.75} \cdot E}{(R/t)^{1.25} \cdot (L/R)^{0.5}} \tag{16}$$

Finally, the bending buckling failure condition is defined to happen when the sum of the ratios between applied and critical stresses exceeds unity.

$$\frac{\tau}{\tau_{cr}} + \frac{\sigma}{\sigma_{cr}} < 1 \tag{17}$$

Using this scheme, the analysis of the structure yields a thickness of 4.14 mm for the tube made of aluminium 7075-T6, with an outer radius of 14.1 cm and a length equivalent to the span of the wing (8.21 m) in order to prevent overload, column buckling and shell bending buckling. The mass of the shaft with that thickness would be 84 kg for the wing, which is considerably lower than the mass of the wing presented earlier in the initial preliminary design of section VI.

That being said, this does not include the mass of the such as the leading edge and trailing edge structures, as well as the ribs, that are attached to the wing rotational mechanism which also have to carry all the shear and transfer it to the tubular shaft. These structures were not investigated in the present work, but could also be included in a preliminary design phase, possibly making use of the leading and trailing edge panels for additional load carrying capacity. As the shaft is connected to the airfoil using welding, there is an increased susceptibility of the aluminium tube to galvanic corrosion and to undergo fatigue accelerated by corrosion, but the extent of the impact thereof is deemed to be a topic to be addressed in more detailed design phases. Considering the load carrying capacity, and especially the torsional loads, the tubular beam is evaluated to be the preferable option in contrast to a conventional wingbox. However, the certainty in this claim is rather low due to several extraneous factors unaccounted for in both cases.

XII. Conclusion and recommendations

The current discussion provides a baseline approach that can be used in the preliminary design for crashworthiness of a long-range eVTOL. Such design approach should be extended for other types of eVTOL belonging to short- and mid-range, which show a large variety in terms of types of structural component and structural layouts. The methodology can be extended to include more structural components of the wing structures, such as the leading edge, trailing edge, and ribs. The fuselage structural analysis for static and fatigue loads should be included, and a quantitative assessment of the crashworthiness behaviour already during the preliminary design phase remains a challenge.

In addition to the above, the wing rotation mechanism can be designed even further, given the parameters of the circular shaft in section XI. As the requirements of the wing rotation mechanism are defined, the components necessary for the functionality of this mechanism may be selected and the best architecture determined.

Moreover, the mass estimation methods for the subsystem level (ie. Class II) may be improved, given that more details about the geometry of the structural components are known. Currently, Cessna's method is employed for the weight estimation, and this semi-empirical method is derived using data from more conventional aircraft vehicles. The accuracy of Cessna's method for non conventional configurations such as the Wigeon, which also includes tilting wing mechanisms, must be further investigated and verified.

Furthermore, the topic of design for crashworthiness based on a building block approach should be further explored; whereby, in a coupon level, new materials with high energy absorbing capabilities can be further investigated and their impact on the life cycle and passenger safety of eVTOLs investigated already in the preliminary design phase. Additionally, in the structural element and structural assembly levels of such building block approach, the design of all structures related to the energy absorption in crash events should be considered already in the preliminary design phase, in order to reduce the cost for new products and reach optimum levels of safety at minimum life cycle costs.

CRediT authorship contribution statement

K. Wadia, M. Buszek, N. Poliakov: Methodology, investigation, formal analysis, validation, software, writing - original draft preparation, writing - reviewing and editing. **S.G.P. Castro:** Conceptualization, supervision, writing - reviewing and editing.

Acknowledgments

This work has been developed as part of the Design Synthesis and Exercise "Multi-Disciplinary Design and Optimisation of a Long-Range eVTOL Aircraft", given during the Spring quarter in 2021.

We would like to thank our tutor Dr. Saullo Castro and our coaches Davide Biagini and Dr. Ali Nokhbatolfoghahai for their support and guidance throughout this project. Lastly, we would like to thank the rest of our project group, Egon Beyne, Miguel Cuadrat-Grzybowski, Noah Salvador López, Javier Alba Maestre, Koen Prud'homme van Reine, Alejandro Montoya Santamaría and Jakob Schoser.

References

[1] Alba-Maestre, J., Beyne, E., Buszek, M., Cuadrat-Grzybowski, M., Montoya Santamaria, A., Poliakov, N., Prud'homme van Reine, K., Salvador Lopez, N., Schoser, J., and Wadia, K., "Final Report - Multi-Disciplinary Design and Optimisation of a Long-Range eVTOL Aircraft," Tech. rep., Delft University of Technology, 2021. https://doi.org/10.5281/zenodo.5576103.

[2] Alba-Maestre, J., Beyne, E., Buszek, M., Cuadrat-Grzybowski, M., Montoya Santamaria, A., Poliakov, N., Prud'homme van Reine, K., Salvador Lopez, N., Schoser, J., and Wadia, K., "Midterm Report - Multi-Disciplinary Design and Optimisation of a Long-Range eVTOL Aircraft," Tech. rep., Delft University of Technology, 2021. https://doi.org/10.5281/zenodo.5576027.

[3] N., P., E., T., Wei, P. ., and Mitici, M., "A review of current technology and research in urban on-demand air mobility applications," , 2019.

[4] Society, T. V. F., "eVTOL Aircraft Directory," , 2021. URL https://evtol.news/aircraft.

[5] EASA, "EASA Special Condition for VTOL and Means of Compliance," , 2020. URL https://www.easa.europa.eu/document-library/product-certification-consultations/special-condition-vtol.

[6] Findlay, S. J., and Harrison, N. D., "Why aircraft fail," , 11 2002. https://doi.org/10.1016/S1369-7021(02)01138-0.

[7] Schijve, J. (ed.), *Designing against Fatigue of Structures*, Springer Netherlands, Dordrecht, 2009, pp. 559–586. https://doi.org/10.1007/978-1-4020-6808-9_20, URL https://doi.org/10.1007/978-1-4020-6808-9_20.

[8] Lipski, A., "Rapid determination of the Wöhler's curve for aluminum alloy 2024-T3 by means of the thermographic method," American Institute of Physics Inc., 2016. https://doi.org/10.1063/1.4965936.

[9] Fujio, Y., Xu, C. N., Sakata, Y., Ueno, N., and Terasaki, N., "Invisible crack visualization and depth analysis by mechanoluminescence film," *Journal of Alloys and Compounds*, Vol. 832, 2020, p. 154900. https://doi.org/10.1016/j.jallcom.2020.154900.

[10] Salvador López, N., Montoya Santamaría, A., and Castro, S. G. P., "Preliminary aerodynamic analysis for the multi-disciplinary design and optimisation of a long-range eVTOL aircraft," *AIAA Scitech 2022 Forum*, American Institute of Aeronautics and Astronautics, Reston, Virginia, 2022.

[11] "Combined Corrosion and Wear of Aluminium Alloy 7075-T6," *Journal of Bio- and Tribo-Corrosion*, Vol. 2, 2016. https://doi.org/10.1007/s40735-016-0042-3.

[12] Roskam, J., *Airplane design Part V: Component Weight Estimation*, DARcorporation, 1986.

[13] Alba Maestre, J., Beyne, E., Buszek, M., Cuadrat-Grzybowski, M., Montoya Santamaria, A., Poliakov, N., Prud'homme van Reine, K., Salvador Lopez, N., Schoser, J., and Wadia, K., "Baseline Report - Multi-Disciplinary Design and Optimisation of Long-Range eVTOL Aircraft," , 2021.

[14] Yang, X., Ma, J., Wen, D., and Yang, J., "Crashworthy design and energy absorption mechanisms for helicopter structures: A systematic literature review," *Progress in Aerospace Sciences*, Vol. 114, 2020, p. 100618. https://doi.org/10.1016/j.paerosci.2020.100618.

[15] Alba-Maestre, J., Prud'homme van Reine, K., Sinnige, T., and Castro, S. G. P., "Preliminary propulsion and power system design of a tandem-wing long-range eVTOL aircraft," *Applied Sciences*, Vol. 11, No. 23, 2021. https://doi.org/10.3390/app112311083.

[16] "HexWeb® A1 and A10 High strength aramid honeycomb Product Data," , 2007. URL https://www.hexcel.com/user_area/content_media/raw/A1A10_eu.pdf.

[17] Dear, J. P., Maruszewska, W., Oh, S. T., and Lee, H., "Energy Absorbing Ability of Sandwich Composite Structures," *Fracture of Nano and Engineering Materials and Structures*, edited by E. E. Gdoutos, Springer Netherlands, Dordrecht, 2006, pp. 1263–1264.

[18] Mair, C., Rezgui, D., and Titurus, B., "Nonlinear stability analysis of whirl flutter in a rotor-nacelle system," *Nonlinear Dynamics*, Vol. 94, 2018, pp. 2013–2032. https://doi.org/10.1007/s11071-018-4472-y.